JOURNAL OF SPACECRAFT AND ROCKETS
Vol. 45, No. 5, September–October 2008

Correlation of Hybrid Rocket Propellant Regression Measurements with Enthalpy-Balance Model Predictions

Shannon D. Eilers* and Stephen A. Whitmore†
Utah State University, Logan, Utah 84322-4130

DOI: 10.2514/1.33804

Currently, the rocket propulsion industry uses an empirical curve fit to predict the hybrid rocket fuel regression rates. These "after the fact" correlations are of little use for predicting the performance of new fuel formulations or grain designs. This paper develops a refined model for predicting hybrid motor fuel regression rates using an enthalpy balance in which fuel-grain ablation heat is balanced by convective heat transfer from the combustion flame zone to the fuel-grain surface. Convective heat transfer is related to the surface skin friction using the Colburn heat-transfer/skin-friction analogy for nonunity Prandtl numbers. Because the Prandtl number is a measure of the relative importance of skin friction and heat transfer within a viscous flowfield, it has a significant effect on the resulting regression rates. The regression model calculates the longitudinally averaged fuel regression rate and is shown to accurately predict chamber pressure, thrust, and specific impulse of a medium-scale hybrid rocket motor. Chemical properties of the combustion products were evaluated using the NASA Chemical Equilibrium with Applications combustion code. Model predictions for a nitrous oxide (N_2O) and hydroxyl-terminated polybutadiene motor are compared with data from a small-scale test firing with a 10.2-cm-diam motor.

Nomenclature

A^*	=	nozzle throat area, cm^2
A_{burn}	=	instantaneous fuel surface area, cm^2
A_c	=	chamber cross-sectional area, cm^2
A_{ox}	=	injector hole area, cm^2
B	=	blowing parameter
$C_{d_{\text{ox}}}$	=	injector discharge coefficient
C_f	=	longitudinally averaged skin-friction coefficient
C^*	=	characteristic exhaust velocity, m/s
c_{f_x}	=	local skin-friction coefficient
$(c_{fx})_{\text{blowing}}$	=	c_f coefficient with blowing adjustment
c_p	=	solid fuel specific heat, J/kg K
c_{p_e}	=	specific heat of oxidizer at flame, J/kg K
D_H	=	hydraulic diameter, cm
G	=	total mass flux, kg/m^{2}s
H	=	convective heat-transfer coefficient
h_v	=	heat of vaporization, J/kg
L	=	length of fuel grain, m
M_c	=	total mass contained in combustion chamber, kg
M_R	=	instantaneous mixture ratio
$\dot{m}_{\text{fuel}}$	=	mass flow rate of fuel, kg/s
$\dot{m}_{\text{nozzle}}$	=	net mass flow rate through nozzle, kg/s
$\dot{m}_{\text{ox}}$	=	mass flow rate of oxidizer, kg/s
$\dot{m}_{\text{propellant}}$	=	mass flow rate of propellant, kg/s
Pr	=	Prandtl number
p_{ox}	=	oxidizer pressure, kPa
p_0	=	stagnation pressure, kPa
$\dot{q}$	=	total heat transfer at surface, J/kg
Re_L	=	longitudinal average Reynolds number
Re_x	=	local Reynolds number
Re_δ	=	boundary-layer Reynolds number
R_g	=	gas constant, J/kg K
R_{port}	=	instantaneous port radius, cm
$\dot{r}$	=	instantaneous regression rate, cm/s
St	=	Stanton number
T_{flame}	=	flame temperature, K
T_{fuel}	=	fuel temperature, K
T_{surface}	=	fuel-grain surface temperature, K
T_0	=	stagnation temperature, K
t	=	time, s
U_e	=	oxidizer velocity at flame boundary, m/s
V_c	=	combustion chamber volume, cm^3
x	=	longitudinal coordinate, cm
γ	=	specific heat ratio
$\Delta h_{\text{surface}}$	=	specific enthalpy difference at fuel surface, (m/s)^2
$\Delta\tau_{12}$	=	correlation time interval between first and second regression thermocouple, s
$\Delta\tau_{13}$	=	correlation time interval between first and third regression thermocouple, s
$\Delta\tau_{23}$	=	correlation time interval between second and third regression thermocouple, s
δ_x	=	Boundary-layer thickness, cm
μ	=	viscosity, kg/ms
μ_{ox}	=	oxidizer viscosity, kg/ms
μ_∞	=	fluid viscosity, kg/ms
ρ	=	density, kg/m^3
ρ_{fuel}	=	fuel density, kg/m^3
ρ_{ox}	=	oxidizer density, kg/m^3
τ_{wall}	=	wall shear stress, kPa

Presented as Paper 5349 at the 43rd AIAA/ASME/SAE/ASEE Joint Propulsion Conference & Exhibit, Cincinnati, OH, 8–11 July 2007; received 31 July 2007; revision received 14 January 2008; accepted for publication 24 February 2008.

*Graduate Research Assistant, Mechanical and Aerospace Engineering Department, 4130 Old Main Hill, University Mail Code 4130. Student Member AIAA.

†Assistant Professor, Mechanical and Aerospace Engineering Department, 4130 Old Main Hill, University Mail Code 4130. Associate Fellow AIAA.

I. Introduction

APPROXIMATELY 70% of all the catastrophic rocket-system failures are attributable to the power plant of the rocket [1]. Reduction of the probability of propulsion failures requires picking the right rocket engine type. There are three major types of rocket engines. Liquid propellant engines use an oxidizer and a separate fuel that are mixed through injectors within the combustion chamber. Solid-propellant motors use a solid-propellant grain that contains both the oxidizer and the fuel. A hybrid motor typically uses a liquid oxidizer such as nitrous oxide or liquid oxygen and a separate solid fuel grain such as rubber or plastic.

Both liquid rocket engines and solid rocket motors can catastrophically explode. For example, the estimate for the space

shuttle's liquid fueled main engines is one explosion every 1530 sorties per engine and, for its solid rocket boosters, one explosion every 1550 sorties per motor. Hence, designers limit the number of such engines to reduce the possibility of explosion. A large number of liquid engines or solid motors increases the chance of a catastrophic failure. On the other hand, according to the U.S. Department of Transportation [2], hybrid motors can be fabricated, stored, and operated without any possibility of explosion or detonation. Other advantages of hybrid rockets include their ability to be stopped, restarted, and throttled; easy (hence, potentially cheaper) ground handling; and relative insusceptibility to grain flaws. Multiple hybrid motors can be used to improve propulsion system reliability by providing redundancy in the case that one hybrid motor fails to produce adequate thrust.

A large hybrid motor built by Space Development Corporation (San Diego, California) powered the Scaled Composites Spaceship One® to the first privately funded manned spaceflights, and the eventual *X*-prize championship. The future of privately funded manned space flight will be closely tied to the improvement, characterization, and development of hybrid rocket systems. Figure 1 shows a typical hybrid motor layout [3]. The relative positions of the oxidizer tank, pressurant tank, fuel chamber, and nozzle depend on the specific motor design. Some designs rely on the natural vapor pressure of the oxidizer to feed the injector, and the pressurant tank is eliminated from the design altogether.

The advantages of hybrid technology, however, also come with their own set of technological challenges. Prominent among these challenges is the characterization of regression rate scaling effects. Hybrid rocket technology is still a developing field that makes small-scale tests of potential fuel combinations invaluable to the development of hybrid propulsion systems. However, hybrid motor combustion parameters are complex, and the scaling effects of regression rate and burn pattern are still not well understood. Some research has been done in an attempt to establish similarity conditions for small-scale firings with full-scale counterparts, but this research has primarily involved testing of only very small lab-scale motors. Extrapolation of these parameters to actual flight scale hybrid motors is difficult, and mistakes can be costly.

Currently, the rocket propulsion industry uses an empirical power-law curve fit known as St. Robert's Law to predict solid-propellant and hybrid rocket fuel regression rates [4–6]. This method requires multiple tests of a given fuel or grain configuration to determine the coefficients. Additionally, these relations do little to aid in the prediction of performance of new fuel formulations or grain designs. This paper develops a refined model for predicting the motor regression rates using an enthalpy balance, where the ablation heat of the fuel grain is balanced by the convective heat transfer from the combustion flame zone to the fuel-grain surface. The regression model, based on the longitudinally averaged fuel regression rates, is shown to reasonably predict the chamber pressure, thrust, and specific impulse performance of a 10.2-cm-diam hybrid rocket motor.

II. Enthalpy-Balance Regression Model History

Although the basic structure of an enthalpy-based fuel regression model for hybrids was proposed in the 1960s by Marxman and Gilbert [7], the generic form of the original model is not often used due to difficulty in predicting required fluid parameters and deviations of experimental data from this model. However, the original model derivation remains a classic examination of the underlying physical drivers of both regression rate and combustion behavior in the hybrid rocket. For this reason, an examination of the original enthalpy-based model presented by Marxman and Gilbert has great value.

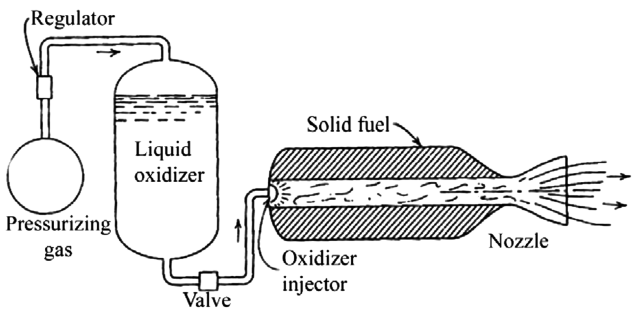

Fig. 1 Typical hybrid motor hardware layout.

The principle assumption made by Marxman and his colleagues was that regression rates in a hybrid rocket are dominated by thermal diffusion and not chemical kinetics [8]. Modifications to the direct regression rate relation based upon radiant heat transfer to the fuel surface were also proposed but were found to be negligible for hybrid rocket fuels free of metallic particles. Given these simplifications, the following flat-plate heat-transfer-based regression-rate equation was proposed to describe the regression rate behavior in hybrid rocket motors:

$$\dot{r} = \frac{0.036}{\rho_{\text{fuel}}} \left(\frac{\mu_\infty}{x}\right)^{0.2} \frac{G^{0.8} B^{0.23}}{Pr^{0.15}} \tag{1}$$

Since the original regression rate proposed by Marxman, a great deal of research has been done on hybrid rocket regression correlations, including the effects of gas kinetics, oxidization, and radiant heat transfer. Specifically, work by Strand et al. [6] and later Chiaverini et al. [5] has further refined the enthalpy-based model developed by Marxman. These studies also tended to show that experimental coefficients in these equations, specifically the exponents on mass flux and the blowing coefficient, are substantially different from the theoretical values derived in the classical relation. Unfortunately, the bulk of regression rate research has often shifted from refining enthalpy-based regression models to creating empirical, St. Robert's Law-based regression rate correlations despite the apparent inability of these models to predict scaling effects or even accurate instantaneous regression rates [5]. The former American Rocket Company suggested that full flight scale motors should be tested as early in a development phase as possible to accommodate for the inabilities of empirical relations to accurately interpolate hybrid rocket motor behavior to the large scale [9]. Because of the inadequacies of both the current extent of published regression rate data and the relative immaturity of "workable" hybrid rocket regression rate models, the authors of this paper believe reexamination and validation of enthalpy-based regression models to be an impediment toward the large-scale integration of hybrid rocket technology in the aerospace industry.

III. Motor Combustion and Regression Model Development

This section develops the motor combustion model. A regression model based on an enthalpy balance from the surface of the fuel grain to the flame zone is developed first. This regression model is used to develop the chamber pressure response equation based on choking mass flow at the throat and the propellant mass flow through the combustion chamber. Finally a thermochemical model for the combustion is developed. This model is used to generate lookup tables for use in the regression and combustion pressure models.

A. Fuel Regression Model

Sutton and Biblarz ([3], p. 733) outlines the basic structure of the enthalpy-balance regression rate model used for this analysis. For high-pressure hybrid combustion, fuel surface regression has been shown to be a function of turbulent boundary-layer heat transfer in a variety of studies. Therefore, for this model it is assumed that a turbulent flame zone close to the fuel surface dominates combustion in hybrid rocket motors. Boundary-layer mixing creates a region in which oxidizer flow from the center of the motor combustion port mixes with vaporizing solid fuel leaving the fuel wall. Close to the fuel wall is the flame zone, where the combustion of fuel and oxidizer primarily takes place. Heat transfer from this zone to the solid fuel

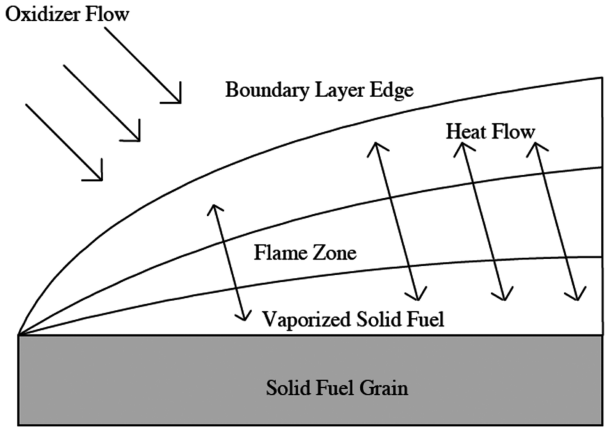

Fig. 2 Flame zone typical to hybrid rocket combustion.

grain drives the regression rate behavior of hybrid rocket motors. This process is depicted in Fig. 2.

The enthalpy-based regression model starts with the examination of heat transfer in a control unit on the fuel-grain surface. Heat transfer from convection is directly related to the fuel regression rate through

$$\dot{q} = \rho_{\text{fuel}} \dot{r} h_v \tag{2}$$

The heat transfer from convection is equated to the heat transfer across the solid fuel grain at the fuel-grain surface. Assuming an approximately cylindrical port geometry, this enthalpy balance gives

$$\rho_{\text{fuel}} \dot{r} h_v = H(T_{\text{flame}} - T_{\text{surface}}) \tag{3}$$

In Eq. (3), $\dot{r}$ is the linear rate of change of the fuel port radius, equivalent to the rate of fuel-grain regression. For a noncylindrical port geometry, the port radius can be approximated by one-half of the hydraulic diameter $D_H = (4A_c/\pi)^{1/2}$. Figure 3 illustrates the fuel regression for a particular cross section within the motor.

The convective heat-transfer coefficient in Eq. (3) is expressed in terms of the Stanton number:

$$H = c_{p_e} \rho_e U_e St \tag{4}$$

Equation (4) is substituted into Eq. (3) to give

$$\rho_{\text{fuel}} \dot{r} h_v = St \rho_e U_e c_{p_e} (T_{\text{flame}} - T_{\text{surface}}) = St \rho_e U_e \Delta h_{\text{surface}} \tag{5}$$

where U_e, ρ_e, and c_{p_e} are the oxidizer velocity, density, and specific heat at the edge of the flame boundary, respectively. The Δh term is the enthalpy difference between the gas at the surface of the fuel grain and the gas within the flame zone. Because the internal flow in a hybrid motor of this size is highly turbulent, Stanton number can be related to the local skin-friction coefficient and turbulent Prandtl number using the Colburn heat-transfer/skin-friction analogy for nonunity Prandtl number [10,11]:

$$St = \frac{c_{f_x}}{2} Pr^{-\frac{2}{3}} \tag{6}$$

Equation (6) is a modification of the original Reynolds analogy (valid only for unity Prandtl number) and is derived from the fact that the velocity and temperature profiles within the laminar sublayer (within the fuel ablation zone) are linear with height above the surface. The Prandtl number is a measure of the relative importance of skin friction and heat transfer within a viscous flow field. For laminar flowfields, the Prandtl number can vary from nearly zero to values greater than 1000. For turbulent flowfields, its value is limited to less than unity. Depending on the working fluid, for typical pipe flows, the turbulent Prandtl number is approximately constant and has a magnitude ranging from approximately 0.5 to 1.0 [12]. For the hybrid motor, the mean gaseous products within the chamber are strongly influenced by the propellant mixture ratio and the chamber pressure. A 50–100% variation in turbulent Prandtl number can be observed over the operating range of the motor. Thus, for this combustion model, the Prandtl number is considered a function of motor mixture ratio and chamber pressure. Modeling of the Prandtl number and other fluid properties will be discussed in detail later in Sec. III.C. Substituting Eq. (6) into Eq. (5) and solving for the regression rate yields

$$\dot{r} = \frac{[\frac{c_{f_x}}{2} Pr^{-\frac{2}{3}}] \Delta h_{\text{surface}} \rho_e U_e}{\rho_{\text{fuel}} h_v} \tag{7}$$

The Reynolds–Colburn analogy is strictly valid only for fixed wall boundaries with no out gassing, and a correction factor for surface blowing is needed to account for the mass addition of the vaporized fuel. This correction for an actively evaporating fuel surface is presented by Lees [13] as

$$(c_{f_x})_{\text{blowing}} = 1.27 \left(\frac{\Delta h_{\text{surface}}}{h_v} \right)^{-0.77} c_{f_x} \tag{8}$$

Substituting Eq. (8) into Eq. (7) and collecting terms gives the corrected form of the regression rate equation:

$$\dot{r} = \frac{0.635 (\frac{\Delta h_{\text{surface}}}{h_v})^{0.23} [c_{f_x} Pr^{-\frac{2}{3}}] \rho_e U_e}{\rho_{\text{fuel}}} \tag{9}$$

Equation (9) is generally valid at each longitudinal point along the fuel grain, and, clearly, the boundary layer within the tube will grow until fully developed channel flow is reached. This boundary-layer growth process is depicted in Fig. 4.

The fuel-grain geometries under consideration for this model typically have very low aspect ratios with length to diameter ratios less than 20, and fully developed channel flow is not generally reached in the port length. Thus, for this analysis, a simple empirical skin-friction model based on flat-plate boundary-layer theory was used in lieu of a fully developed model for pipe-flow skin friction. Although the authors recognize that the evolution of the port boundary layer is an extremely complex phenomenon, this simple longitudinal model for turbulent flow shows good agreement with the Karman–Schonherr (K–S) model. The K–S skin-friction model is still the choice of naval architects for modeling the development of skin friction for three-dimensional boundary layers on ship hulls [14]. Furthermore, Mottard and Loposer [15] verified the applicability of this model to three-dimensional flows. Thus, the model used for this analysis was developed based on the empirical relationship for boundary-layer thickness:

$$\delta_x = \frac{0.38x}{(Re_x)^{1/5}} = \frac{0.38x}{(\frac{\rho U_e x}{\mu})^{1/5}} \tag{10}$$

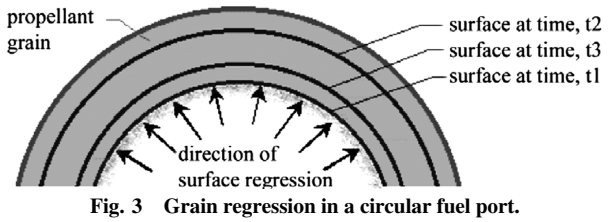

Fig. 3 Grain regression in a circular fuel port.

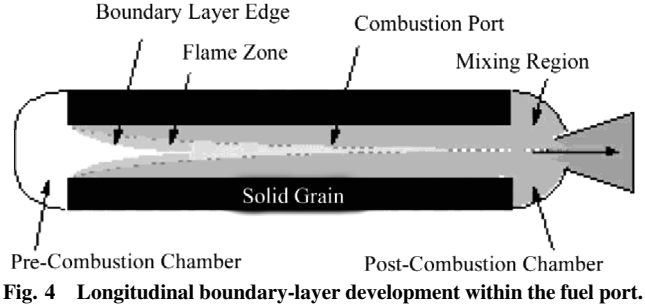

Fig. 4 Longitudinal boundary-layer development within the fuel port.

and the Blasius formula for turbulent wall shear stress ([10], pp. 429–430):

$$c_{f_x} = \frac{\tau_{\text{wall}}}{\frac{1}{2}\rho U_e^2} = \frac{0.0465}{(Re_x)^{1/4}} = \frac{0.0465}{(\frac{\rho U_e \delta_x}{\mu})^{1/4}} \tag{11}$$

In Eq. (11), Re_x is the Reynolds number based on the longitudinal distance down the chamber, δ_x is the local boundary-layer thickness, U_e is the velocity at the edge of the boundary layer, and ρ and μ are the density and dynamic viscosity of the combustion products. Equations (9) and (10) are valid for $10^6 < Re_x < 10^7$. Substituting Eq. (10) into Eq. (11) and collecting terms

$$c_{f_x} = \frac{\tau_{\text{wall}}}{\frac{1}{2}\rho U_e^2} = \frac{0.0592}{(Re_x)^{1/5}} \tag{12}$$

Equation (11) is integrated along the length of the port to give an averaged value for the skin-friction coefficient:

$$C_F = \frac{1}{L}\int_0^L \frac{0.0592}{(Re_x)^{1/5}}\,\mathrm{d}x = \frac{0.074}{(Re_x)^{1/5}} \tag{13}$$

The resulting longitudinal mean skin-friction model is

$$C_f = \frac{0.074}{[Re_L]^{\frac{1}{5}}} \tag{14}$$

where Re_L is Reynolds number based on chamber length. For a typical moderate-size hybrid motor, Reynolds number will vary from 2–5 million Reynolds units. The oxidizer mass flux term $\rho_e U_e$ is related to the instantaneous cross-sectional combustion chamber area and the mass flow rate of oxidizer out of the injector with the relation

$$\rho_e U_e = \frac{\dot{m}_{\text{ox}}}{A_c} \tag{15}$$

where, based on the oxidizer injector geometry

$$\dot{m}_{\text{ox}} = A_{\text{ox}} C_{d_{\text{ox}}} \sqrt{2\rho_{\text{ox}}(p_{\text{ox}} - p_0)} \tag{16}$$

Substituting Eqs. (14–16) for skin-friction coefficient and oxidizer mass flux into Eq. (9) derives an approximate model for the longitudinally averaged regression rate along the length of the fuel port:

$$\dot{r} = \frac{0.047}{Pr^{\frac{2}{3}}\rho_{\text{fuel}}}\left(\frac{c_p[T_0 - T_{\text{fuel}}]}{h_v}\right)^{0.23} \times \left[\frac{A_{\text{ox}} C_{d_{\text{ox}}}}{A_c}\sqrt{2\rho_{\text{ox}}(p_{\text{ox}} - p_0)}\right]^{\frac{4}{5}}\left(\frac{\mu_{\text{ox}}}{L}\right)^{\frac{1}{5}} \tag{17}$$

The total mass flow of the fuel being generated by the regressing fuel is simply

$$\dot{m}_{\text{fuel}} = A_{\text{burn}} \cdot \rho_{\text{fuel}} \cdot \dot{r} \tag{18}$$

B. Chamber Pressure Model

As the fuel begins to burn, the combustion process produces high temperature gases that escape through the nozzle throat. Assuming the nozzle throat chokes immediately, the generated gases cannot escape as fast as they are produced, and pressure within the fuel chamber builds. The time response of this chamber pressure growth can be calculated by a balance between the gases coming into the fuel port and the gases leaving through the choked nozzle:

$$\frac{\partial}{\partial t}M_c = \frac{\partial}{\partial t}[\rho_c]V_c + \rho_c\frac{\partial}{\partial t}[V_c] = [\dot{m}_{\text{fuel}} + \dot{m}_{\text{ox}}] - \dot{m}_{\text{nozzle}} \tag{19}$$

After using the ideal gas law to rewrite density in terms of chamber pressure and temperature and rearranging, this becomes

$$\frac{\partial p_0}{\partial t} = \frac{R_g T_0}{V_c}[\dot{m}_{\text{fuel}} + \dot{m}_{\text{ox}}] - \frac{R_g T_0}{V_c}\dot{m}_{\text{nozzle}} - \frac{p_0}{V_c}\frac{\partial}{\partial t}[V_c] \tag{20}$$

Assuming the nozzle chokes immediately after the initiation of combustion, the change in mass of the combustion chamber can be expressed in terms of the general nozzle mass flow equation, the regression rate, and the oxidizer mass flow:

$$\frac{\partial p_0}{\partial t} = \frac{R_g T_0}{V_c}[\rho_{\text{fuel}} A_{\text{burn}}\dot{r} + A_{\text{ox}} C_{d_{\text{ox}}}\sqrt{2\rho_{\text{ox}}(p_{\text{ox}} - p_0)}] - \frac{R_g T_0}{V_c}\left[\frac{p_0 A^*}{\sqrt{T_0}}\sqrt{\frac{\gamma_0}{R_g}\left(\frac{2}{\gamma+1}\right)^{\frac{\gamma+1}{\gamma-1}}}\right] - \frac{p_0}{V_c}\frac{\partial}{\partial t}[V_c] \tag{21}$$

Noting that the time derivative of the chamber volume is simply equal to the regression rate multiplied by the instantaneous burn area, this becomes

$$\frac{\partial p_0}{\partial t} = \frac{A_{\text{burn}}\dot{r}}{V_c}[\rho_{\text{fuel}} R_g T_0 - p_0] - p_0\left[\frac{A^*}{V_c}\sqrt{\gamma R_g T_0\left(\frac{2}{\gamma+1}\right)^{\frac{\gamma+1}{\gamma-1}}}\right] + \frac{R_g T_0}{V_c}A_{\text{ox}} C_{d_{\text{ox}}}\sqrt{2\rho_{\text{ox}}(p_{\text{ox}} - p_0)} \tag{22}$$

The growth of the port radius is described by

$$\frac{\partial R_{\text{port}}}{\partial t} = \dot{r} \tag{23}$$

and the instantaneous chamber volume is

$$V_c = \pi R_{\text{port}}^2 L \tag{24}$$

The instantaneous burn area and combustion port area can be calculated in a similar fashion from

$$A_{\text{burn}} = 2\pi R_{\text{port}} L \tag{25}$$

$$A_c = \pi R_{\text{port}}^2 \tag{26}$$

Equations (16–18), (22), and (23) are integrated as a system with the state vector containing combustion pressure, instantaneous combustion port radius, and the total masses of fuel and oxidizer consumed by the system. These equations allow the dynamic nature of the combustion process to be modeled as a function of time.

For a fixed oxidizer mass flow, the properties of the combustion gasses will change as the port radius grows larger and the mixture ratio becomes increasingly richer. For a fixed oxidizer mass flow, the properties of the combustion gasses will change as the port radius grows larger. Based on Eqs. (16–18), it can be shown that the effective mixture ratio of the rocket is

$$\begin{aligned} M_R &= \frac{\dot{m}_{\text{ox}}}{\dot{m}_{\text{fuel}}} = \frac{A_{\text{ox}} C_{d_{\text{ox}}}\sqrt{2\rho_{\text{ox}}(p_{\text{ox}} - p_0)}}{A_{\text{burn}} \cdot \rho_{\text{fuel}} \cdot \dot{r}} \\ &= \frac{A_{\text{ox}} C_{d_{\text{ox}}}\sqrt{2\rho_{\text{ox}}(p_{\text{ox}} - p_0)}}{A_{\text{burn}} \cdot \rho_{\text{fuel}} \cdot \frac{0.047}{P_r^{\frac{2}{3}}\rho_{\text{fuel}}}\left(\frac{c_p[T_0 - T_{\text{fuel}}]}{h_v}\right)^{0.23}\left[\frac{A_{\text{ox}} C_{d_{\text{ox}}}}{A_c}\sqrt{2\rho_{\text{ox}}(p_{\text{ox}} - p_0)}\right]^{\frac{4}{5}}\left(\frac{\mu_{\text{ox}}}{L}\right)^{\frac{1}{5}}} \\ &= 21.28 P_r^{\frac{2}{3}}\left[\frac{A_c^{\frac{4}{5}} A_{\text{ox}}^{\frac{1}{5}}}{A_{\text{burn}}}\right]\frac{(C_{d_{\text{ox}}}\sqrt{2\rho_{\text{ox}}(p_{\text{ox}} - p_0)}\frac{L}{\mu_{\text{ox}}})^{\frac{1}{5}}}{(\frac{c_p[T_0 - T_{\text{fuel}}]}{h_v})^{0.23}} \end{aligned} \tag{27}$$

Modeling the mixture ratio in this form allows for the computation of combustion product properties at every time step using an equilibrium analysis method.

C. Modeling of the Combustion Product Properties

The motor modeled in this paper burns a combination of liquid nitrous oxide at saturation conditions and hydroxyl-terminated polybutadiene (HTPB). For this analysis, the equilibrium gas-chemistry code Chemical Equilibrium with Applications (CEA) [16] was used to model the combustion products. The CEA code was developed at NASA Glenn Research Center, and has been successfully applied for the analysis of rocket combustion, detonation, and flow across nonadiabatic shock waves. The code

posits chemical reactions across the shock wave and then minimizes the Gibbs free energy [17] to reach thermodynamic and transport properties at chemical equilibrium. The CEA code has extensive internal libraries for gas thermodynamic and transport properties including standard and nonstandard temperature and pressure conditions. Unfortunately, the CEA thermochemical database does not have an entry for HTPB, and the fuel-grain properties, including the atomic mole-fraction formula and enthalpy of formation, must be externally input to the program. Further complicating the problem is the fact that polymer properties, including enthalpy of formation, density, tensile strength, and ablation temperature, depend on the molecule chain length and shape, and these variables can be significantly different for each polymer molecule [18]. Even the effects of the "cooking" process for the same material brand name can result in two samples with drastically different properties. A typical molecular formula for the cured HTPB polymer is approximated by [19]

$$\text{HTPB} = C_4H_{5.9872}O_{0.03162} \tag{28}$$

These atomic mole fractions are in contrast to the pure butadiene gas molecular formula of C_4H_6. The enthalpy of formation is approximately -12.42 kJ/kg · mol.[‡]

For this analysis, the thermodynamic properties of the combustion products including the ratio of specific heats γ, molecular weight, adiabatic flame temperature T_{flame}, viscosity μ, Prandtl number Pr, and characteristic exhaust velocity C^* output by CEA were stored as a function of chamber pressure and mixture ratio and were evaluated at the beginning of each data frame using a two-dimensional table lookup. The flame temperature was scaled by the square root of an assumed combustion efficiency ($\eta^* \sim 0.98$ nominal) to get the combustion chamber temperature. The gas constant and mixture-specific heats were computed from the results of these table lookups. Figure 5 shows these properties plotted as a function of mixture ratio for combustor pressures varying from 100 kPa to 10,000 kPa. Clearly, the optimal mixture ratio for this propellant combination is in the vicinity of 6. The inflection points on the specific heat ratio and Prandtl number curves are a result of the formation of complex alcohol molecules in the combustion products at very fuel rich mixture ratios.

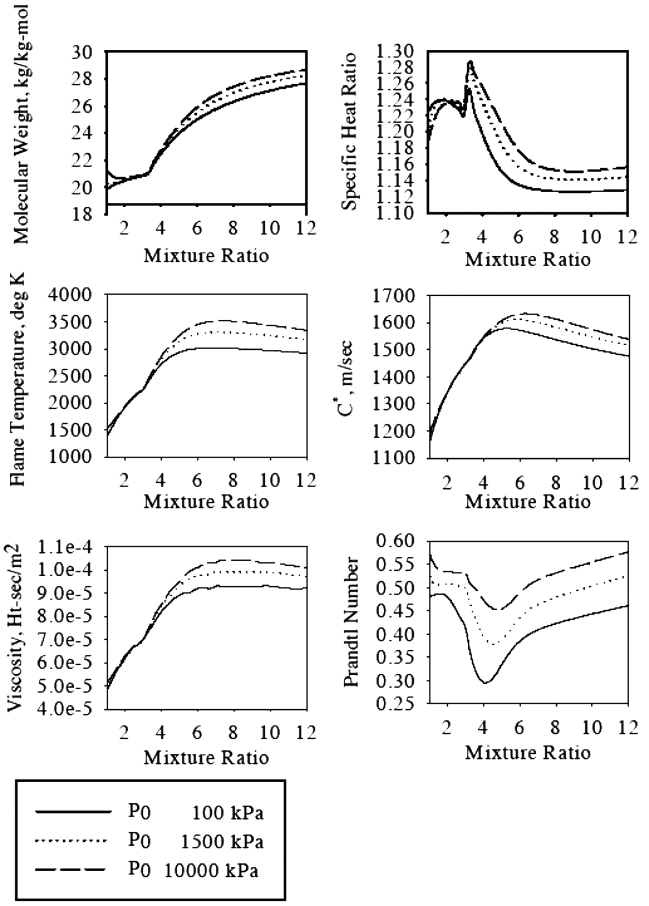

Fig. 5 Thermodynamic and transport properties for HTPB/nitrous oxide combustion.

IV. Experimental Data Collection

Experimental data was collected from two separate burns of a small-scale 10.2 cm hybrid rocket motor. This motor was built and tested as partial fulfillment of the requirement for a senior design project at Utah State University. Motor construction, instrumentation, test procedures, and results from two test firings will be presented in this section. Results from the two tests will be compared with performance predictions based on the combustion model developed in the preceding section.

A. Motor Construction

As mentioned in the preceding section, the 10.2 cm motors used nitrous oxide and HTPB as propellants. The HTPB fuel was manufactured using commercially available products: Arco R45M polybutadiene resin and PAPI 94® curative. Arco R45M is polybutadiene diol manufactured by Sinclair Petrochemicals Inc.'s Arco Division. The resin has a polymerization factor of approximately 45 and a molecular weight of 2745 kg/kg · mol [20]. PAPI 94 is a polymethylene polyphenylisocyanate produced by Dow® Plastics, Inc. The formulation contains methylene diphenylene diisocyanate (MDI) in proprietary proportions. The curative has an average molecular weight of 290 kg/kg · mol. The nitrogen, carbon, oxygen (NCO) bonds in the MDI react with the hydroxyl (OH) terminations in the polybutadiene resin to cure the fuel grain. For best grain set properties, the curative and resin are mixed in a 1:8 weight ratio [21]. The resin and curative were mixed in a commercial paint mixer that was sealed and fitted so that the fuel mixture could be placed under a vacuum during the mixing process. The vacuum was used to remove gas bubbles created in the fuel grain during the mixing process.

The motor casing used for these test fires was constructed of an aluminum tube, 1.016 m in length and 10.2 cm in diameter. The HTPB propellant was cast into a thin-walled (0.28 cm) polyvinyl chloride pipe that served as a removable motor cartridge. The propellant in the motor cartridge could be cast externally to the motor casing and then inserted when the fuel grain was completely cured. This cartridge design allows for quick removal of both the nozzle and the fuel cartridge so that multiple grain geometries can be tested in a single day. After each test firing, the motor cartridge was removed and cut lengthwise for burn-pattern inspection. The internal propellant grain presented approximately 84 linear cm of burnable surface.

The nozzle was manufactured from a single piece of graphite. The nozzle throat diameter is 2.76 cm and has an expansion ratio of 5.566. The nozzle contour follows a partial bell, with an end-plane divergence half-angle of 14 deg. The nozzle fits internally into the fuel cartridge that fits inside the motor casing. The nozzle was held in place by a retaining ring at the end of the motor cartridge. The N_2O injector was an impinging "showerhead" design. In total, 18 injector ports approximately 0.16 cm in diameter were drilled into the injector head. This port configuration resulted in an oxidizer injection area of approximately 0.356 cm^2. The oxidizer system was not actively pressurized and instead relied on the natural vapor pressure of the nitrous oxide in the propellant tank.

B. Measurements and Instrumentation System

For the first test firing, the initial port diameter was approximately 2.6 cm. As will be discussed later, this initial diameter was expanded

[‡]Zakirov, V., "Hybrid Propellants-Fuels," http://www.tsinghua.edu.cn/docsn/lxx/mainpage/a/Web/index_files/page0009.htm [retrieved 14 June 2007].

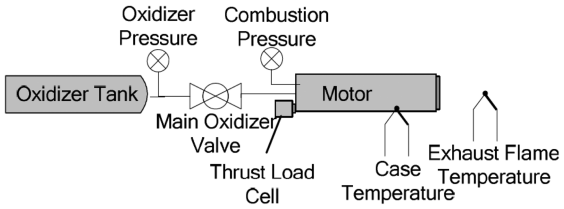

Fig. 6 Test 1 motor instrumentation components.

to approximately 5.1 cm for the second test firing. For the first test firing, combustion pressure, oxidizer pressure, thrust, case temperature, and exhaust flame temperature were measured. The test setup is depicted in Fig. 6, and the corresponding sensors are listed in Table 1. Oxidizer pressure was measured upstream of the main oxidizer valve. Combustion pressure was measured from a port in the motor cap on the forward end of the combustion chamber. The motor was fixed to a test sled on a portable test trailer, and thrust was measured with a strain gauge load cell at the forward end of this test sled. Thermocouples were fastened to the outside of the motor casing and to a steel spar positioned in the exhaust plume. The thermocouple (TC) on the motor case was used to detect the presence of any abnormal temperature spikes during the burn, an indication of possible imminent burn through of the motor casing. The thermocouple situated in the exhaust plume was positioned in an attempt to gauge the exit temperature of the motor configuration before the destruction of the thermocouple. Reference temperature was sensed using a three-wire resistance temperature detector (RTD) inside of the TC connector block.

For the second test fire, 12 type-K thermocouples were embedded in the fuel grain in an attempt to retrieve instantaneous regression rate measurements over the burn duration. Groups of 24-gauge, fine bead, type-K thermocouples were placed at intervals of 10 in. measured axially along the combustion chamber. Three thermocouples each were placed on the forward and aft positions, and six thermocouples were placed in the center. The thermocouple wires were run along the inside of the motor casing through a simple sealed pass through installed in the motor cap. Drilling 12 16 cm holes axially through a grade 2, 1.27 cm steel bolt created this pass through. An O-ring sealed the bolt on the inside of the motor cap, and the thermocouple wires were sealed in place using high-temperature epoxy on the combustion chamber side of the motor cap and cyanoacrylate on the external side. This pass through was then simply bolted through a hole in the motor cap. Figure 7 shows the general placement of the fuel-grain thermocouples, and the thermocouples as attached to the mounting bracket cast into the fuel grain.

The measurement system was completed using a National Instruments Compact Fieldpoint® intelligent control and acquisition system [22]. Two separate Fieldpoint modules, the cFP-AI-118 and the cFP-AI-112, were used for data collection. The 16-bit cFP-AI-118 was used to collect outputs from the MSI 600 pressure transducers and the OMEGA LLCB 1000 lbf load cell. The 16 bit, lower range cFP-AI-112s were used to retrieve thermocouple voltage. The Fieldpoint system was situated on the test trailer, and data was broadcast back over Ethernet to a remote, data-logging laptop. The instrumentation set up for the second test fire was similar to that to the first test fire except that the 12 thermocouples occupied the AI-118 modules, and the pressure transducers and load cells were measured with an AI-112. Additionally, the Fieldpoint system was connected to a data-logging laptop directly with a crossover cable rather than through a hub and avoided reliability issues previously experienced with a commercial Ethernet hub.

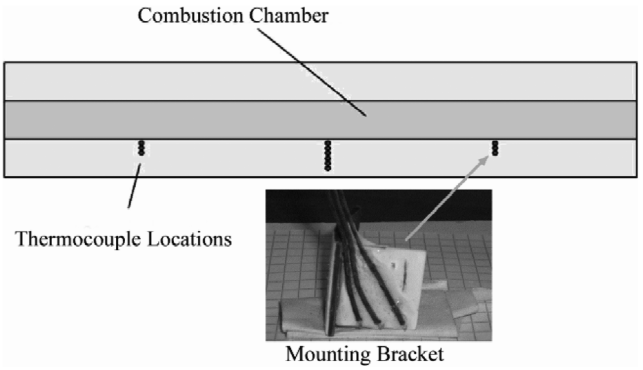

Fig. 7 Thermocouple locations for second static firing.

Fig. 8 Typical test firing of the USU 10.2 cm N2O/HTPB hybrid motor.

C. Rocket Fire Control System

Rocket control was managed via a second laptop and an RF-link to a custom-built controller. The motor combustion was initiated using one of two small solid ammonium nitrate/magnesium rockets imbedded in the motor injector cap. The ignition motors were initiated via an electrical pulse across a nichrome ignition wire. The test sequence would open the oxidizer control valve and then initiate the ignitor. For a typical test fire, the control system would be verified using an inert gas and a spare igniter wire. Once proper operation was confirmed, the system was loaded with nitrous oxide and the firing sequence was repeated. Only one ignitor was needed to start the motor. The second ignition motor was held in reserve for redundancy purposes. Figure 8 shows a collage of a typical 10.2 cm motor test firing including the rocket control system arrangement.

D. Test Results

Figure 9 shows a typical test fire data time history for oxidizer pressure (kPa) measured at the tank, combustion pressure (kPa), and

Table 1 Instrumentation system components

Measurement	Sensor	Fieldpoint module
Combustion pressure	1 k MSI 600 pressure transducer	cFP-AI118
Oxidizer pressure	2.5 k MSI 600 pressure transducer	cFP-AI118
Thrust	OMEGA LCCB-1K	cFP-AI118
Case temperature	Type-K thermocouple	cFP-AI112
Exhaust flame temperature	Type-K thermocouple	cFP-AI112
Reference temperature	3-wire RTD	cFP-RTD122

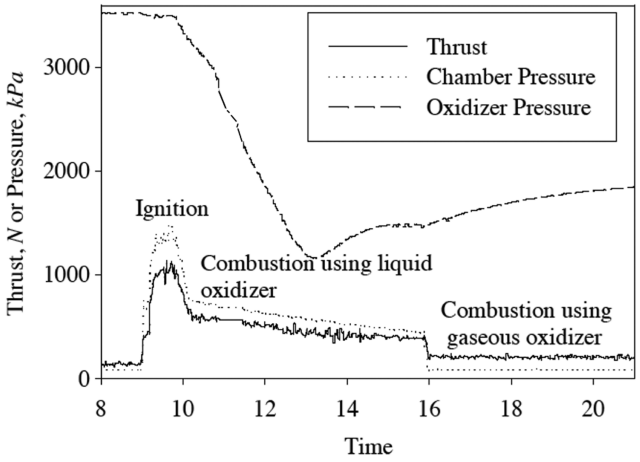

Fig. 9 Time history of 10.2 cm nitrous oxide–HTPB motor test firing.

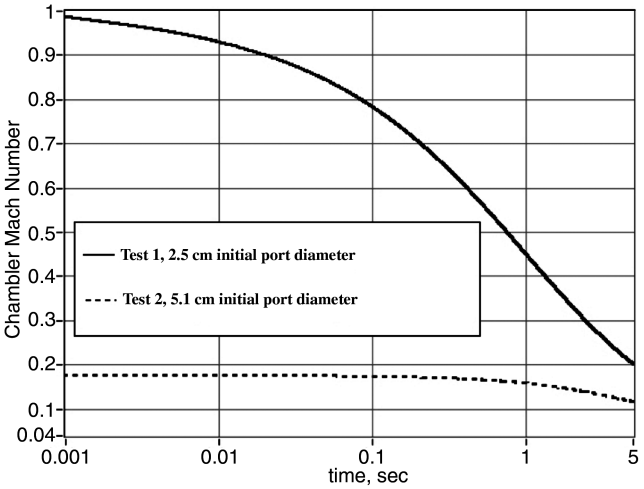

Fig. 10 Initial port Mach number comparison for test 1 and test 2.

thrust (N). Two distinct phases of combustion can be identified. The first stage is characterized by high combustion pressure and thrust. This event is a result of the upstream oxidizer being in the liquid state, resulting in a high oxidizer mass velocity and lean combustion mixture ratio. After approximately 15 s, the liquid nitrous oxide is consumed, and combustion continues using gaseous nitrous oxide. A dramatically reduced oxidizer mass velocity and atypically rich mixture ratio during this period results in dramatically reduced thrust and chamber pressure. Combustion of this form continued for approximately 12 s before the main oxidizer valve was closed, terminating combustion. The large pressure loss between the oxidizer tank pressure measurement, and the sensed chamber pressure is a result of a quick release fitting that was in line with the oxidizer feed line. This fitting resulted in an effective injector discharge coefficient of approximately 0.27. After the fitting was discovered, it was removed for the second test firing.

1. *Fuel-Grain Burn Patterns*

Although the first test fire yielded good data for combustion temperature and thrust, examination of the combustion chamber after the test revealed deep pitting and channeling along the length of the fuel grain. This erosive burning made direct linear measurement of the total fuel regression impossible and posed a potential hazard to the structural integrity of the motor. This chaotic burn pattern was likely caused by a combination of two factors: 1) air bubbles in the fuel grain, or 2) high initial chamber flow Mach numbers. The bubbles in the fuel grain were a result of the fuel mixing and curing process that was employed for the first test. The vacuum pump that was used to degas the fuel had insufficient power to completely degas the mixture. The high initial fuel combustion port Mach numbers were a result of the small initial port diameter (2.5 cm) for the first test firing. The initial port diameter was actually slightly smaller than the nozzle throat and resulted in choked flow near the aft end of the fuel grain. This high initial Mach number resulted in compressible boundary-layer heating and produced excessive frictional shear and heat transfer at the fuel-grain walls. This high initial heat transfer coupled with the weakened fuel grain caused by the imbedded gas bubbles resulted in erosive burning.

In an attempt to remedy this erosive burning issue, two solutions were employed simultaneously. First, a better fuel degassing procedure was employed during the casting process. To aid the degassing procedure, a commercial heating, ventilation, and air conditioning pump was used in place of an older legacy vacuum pump, and a much deeper vacuum on the mixing chamber was achieved. The new pump supplied a vacuum to a depth of almost 30 in. of mercury, whereas the older pump was only capable of a vacuum to 28 in. of mercury. Using this method, a fuel casting visually free of bubbles or voids and a density of approximately 930 kg/m^3 was produced. The fuel used in the first casting had a density of approximately 860 kg/m^3 and had visible bubbles and defects. Second, and likely more important, a larger initial port diameter was used for the second test fire. Increasing the combustion chamber diameter substantially lowered the initial chamber Mach number and, it was hoped, would reduce erosive burning of the combustion chamber. For the second test, the initial port diameter was increased to approximately 5.1 cm. Figure 10 compares the calculated initial mach numbers for the 2.5 and 5.1 cm port diameters. With the small port, the initial flow is choked and then gradually begins to trail off as the chamber enlarges. Eventually, the Mach number approaches that of the larger port after approximately 5 s of burn time. However, by this time the "damage has been done," and the erosive burning pattern has already begun. At this point, the process is irreversible.

Figure 11 compares the burn patterns for the first and second test firings. The motor construction changes between the two test firings resulted in dramatic improvement in the fuel burn properties. In the first burn, the fuel shows deep fissures for nearly 50% of the motor length. In contrast, the burn pattern generated by the second test fire exhibited a smooth and uniform burn free of the chaotic and erosive pattern experienced by the first burn. Also interesting in the second burn are the various stages made evident by the postfire combustion port from the second test fire. For approximately the first 20 cm, the fuel surface is smooth and covered with a thin layer of soot. For the next 15 cm, the surface has a wavy appearance and the soot layer diminishes. After this point, the fuel surface once again becomes smooth, and the surface is soot free. These surface features are likely caused by laminar, transitional, and turbulent flows, respectively. It appears that fully developed pipe flow never occurred in the second burn test and the boundary layer insulates the fuel-grain surface from the turbulent combustion in the center of the chamber.

2. *Grain Regression Rate Measurements*

The burn for the 5.1 cm initial fuel port had such a clean pattern that mean regression rate estimates could be calculated from the posttest fuel grain using direct measurements of the residual HTPB propellant in the motor casing. Figure 12 shows a cross section of the fuel grain showing the fuel port and the residual propellant. Measurements stations as well as the combustion chamber entrance and exit are labeled on this figure.

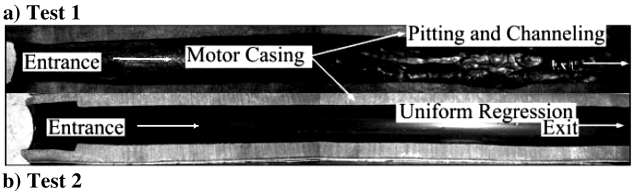

Fig. 11 Comparison of fuel-grain burn patterns, 2.5 cm port (top) and 5.1 cm port (bottom).

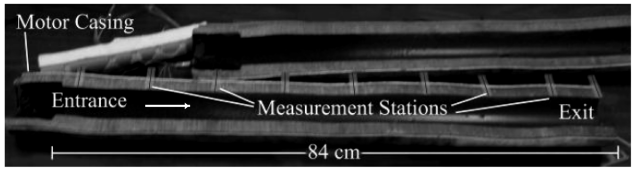

Fig. 12 Posttest fuel-grain cross section.

The total fuel regression during the burn was calculated by measuring the residual HTPB thickness on the upper and lower sides of the chamber cross section, and the total chamber width every 10 cm down the length of the fuel grain. The upper and lower surface propellant thicknesses were summed and then subtracted from the chamber thickness at each measurement section. Subtracting the original port diameter (5.1 cm) gives the total fuel regression at each station. Finally, dividing the total regression data by the motor burn time (6.25 s) calculates the time-averaged rate of regression. Figures 13 and 14 show these regression measurements plotted against longitudinal distance down the chamber along with mean second order trend lines. Figure 13 shows the total regression data. Figure 14 plots the regression rate data. By integrating the second-order trend-line curve fit along the length of the motor and then normalizing by the motor length, the longitudinally averaged regression rate was calculated.

$$\dot{r}_{\text{avg}} = \frac{1}{L_{\text{chamber}}} \int_0^{L_{\text{chamber}}} \left[\sum_{i=1}^{2} a_i x^i \right] \mathrm{d}x = \sum_{i=1}^{2} \frac{a_i (L_{\text{chamber}})^i}{i+1} \tag{29}$$

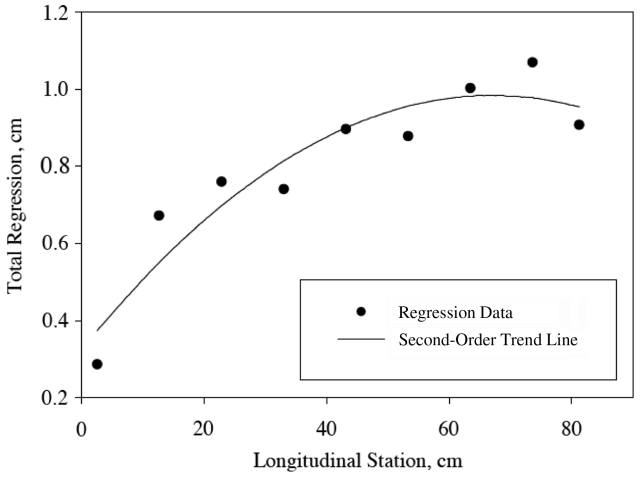

Fig. 13 Longitudinal distribution of fuel-grain regression.

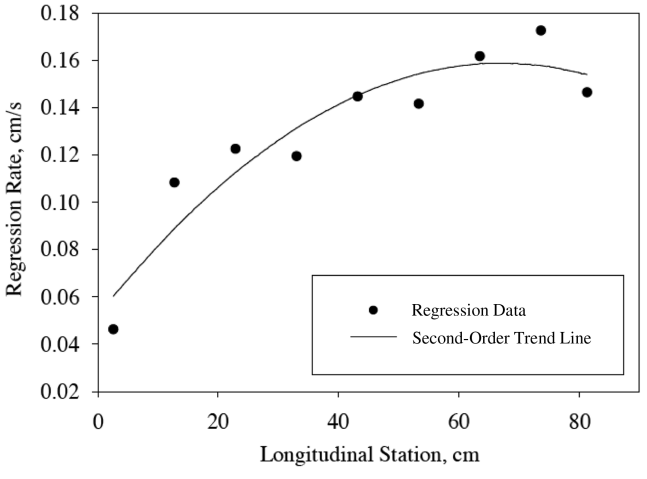

Fig. 14 Longitudinal distribution of fuel regression rate.

Table 2 shows the calculated mean regression and regression rate, the standard errors in the curve fits, and the 95% confidence interval for the data based on the student-t distribution for 8 deg of freedom [23].

In contrast to the well-defined, time-averaged regression rates presented in Table 2, interpretation of the instantaneous regression rates from the imbedded thermocouples is more ambiguous, and the results must be presented with some level of reservation. As mentioned earlier, there were three thermocouple regression arrays embedded in the fuel grain, unfortunately, only the densely populated array near the center of the motor experienced sufficient regression so that multiple TCs were exposed to the flow. Additionally, the embedded TC array induced some localized erosion in the combustion port, leading to an increased regression at the fuel surface near the thermocouples. The channel eroded by these thermocouples can be seen in Fig. 15. Because of the localized regression around the thermocouples in the motor, the instantaneous regression rates calculated from this TC sensor array must be considered as potentially suspect. Clearly, this localized erosion issue emphasizes the need to create a nonintrusive regression rate sensor.

Figure 16 presents the time histories of the three midmotor thermocouples that were exposed to the flow by the fuel-grain regression. Figure 17 shows the relative positions of the thermocouples within the sensor array. Interestingly, both the first and second thermocouples become an open circuit when first exposed to the flow, only to "reweld" at some point later on. The third thermocouple did not create an open circuit because the motor was shut down at 6.25 s. The time intervals between the thermocouple traces was evaluated using by taking the numerical cross correlation [24] of the time history traces for various lag intervals and selecting the lag interval with the maximum correlation. For correlations of the first and second thermocouple with the third thermocouple, the time histories were truncated for temperatures above 760°C. The regression rate was calculated by dividing the correlation lag parameter $\Delta\tau$ by the distances between the thermocouples in the regression array.

Table 3 summarizes the midmotor regression sensor parameters. The regression rates are calculated in three ways: 1) using the maximum correlation time lag ($\Delta\tau_{12}$) for TCs 1 and 2 and the distance separating these sensors, 2) using time lag ($\Delta\tau_{23}$) for TCs 2 and 3 and the distance separating these sensors, and 3) using time lag ($\Delta\tau_{13}$) for TCs 1 and 3 and the distance separating these sensors. Each of the measurements produces remarkably similar results, and these results agree exceptionally well with the mean regression rate data presented in Table 2. Thus, it appears that the localized erosion near the midmotor TC array did not affect the relative regression rate between the individual TCs embedded in the motor grain.

V. Model Comparisons

As mentioned in the preceding section, the first and second test firings mentioned previously burned fuel grains with an initial port diameter of approximately 2.5 and 5.1 cm, respectively. Although the regression rate model used for this analysis is longitudinally averaged, predictions from the numerical model characterize the motor performance reasonably well. However, before the behavior of the model could be validated, specific parameters of the relevant motor system had to be evaluated. First, the injector discharge coefficient for both firings had to be calculated. Although the theoretical discharge coefficient was known, fittings and plumbing losses lead to an effective discharge coefficient substantially different from that estimated. For the first firing, the discharge coefficient was evaluated by integrating Eq. (16), the oxidizer mass flow rate for an injector, over a time-logged pressure differential with a known total mass discharge. Using this method, a discharge coefficient of 0.27 was obtained for the injector. As mentioned in the earlier discussion, this very low discharge coefficient was the result of a quick release fitting in the oxidizer flow path. For the second test fire, less restrictive fittings were used, and the discharge coefficient was estimated using turbulent head loss based on the known

Table 2 Total regression and regression rate statistical data

Parameter	Longitudinal mean value	Standard error in trend line	95% confidence interval about mean
Total regression, cm	0.8054	0.0736	±0.0560
Regression rate, cm/s	0.1299	0.0119	±0.0091

geometry of the oxidizer feed line. Table 4 lists the relevant parameters used for the combustor model calculations.

A. Chamber Pressure, Thrust, and Mixture Ratio Comparisons

The oxidizer system for this test motor relied on the natural vapor pressure of the nitrous oxide in the propellant tank. As a result, a decaying oxidizer pressure drove the upstream injector pressure. This measured oxidizer pressure time history was imported into the motor algorithm and used to calculate the oxidizer mass flow across the injector and the resulting combustor pressure. The predicted motor chamber pressure and thrust are compared with the measured values in Figs. 18–21. Figure 18 plots the chamber pressure comparison for test 1, and Fig. 19 plots the chamber pressure comparisons for test 2. Figure 20 plots the motor thrust comparison for test 1, and Fig. 21 plots the thrust comparison for test 2.

Whereas the predicted chamber pressure and thrust values for test 1 show some considerable disagreement with the measured values, the predictions for test 2 are nearly "dead on." Clearly, the improved burn pattern also improved the model's ability to characterize the combustion process.

Figure 22 compares the predicted burn mixture ratios for the two tests. In both cases, the motors are burning at a richer mixture ratio than is predicted as optimal (Fig. 5).

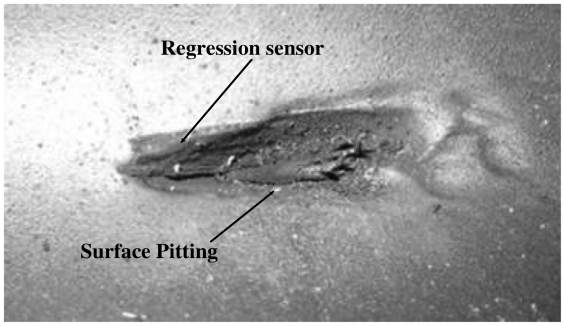

Fig. 15 Localized erosion around type-K thermocouples cast in fuel grain.

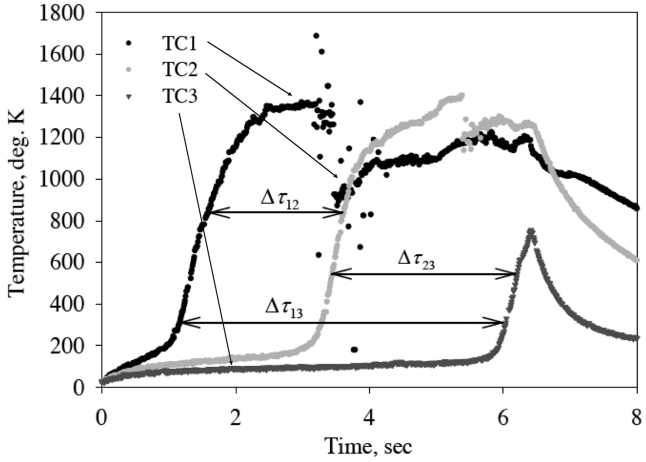

Fig. 16 Time histories of midmotor thermocouples exposed to flow.

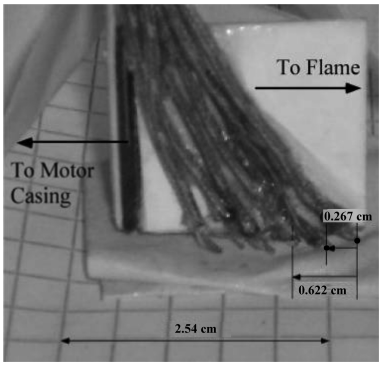

Fig. 17 Midmotor thermocouple array layout.

B. Regression Rate Comparisons

Only data from the second motor test firing are available for comparison with the enthalpy-balance model predictions. The chaotic grain regression in the first test firing made regression rate correlation impossible. Both the time-averaged and instantaneous regression rate data from Tables 2 and 3 will be presented here. Figure 23 presents the regression rate comparisons. In this figure, the hybrid regression rate is plotted as a function of oxidizer mass velocity (oxidizer mass flow divided by cross-sectional area of the motor port) using a log–log axis. The enthalpy-balance model predictions are plotted as dashed gray lines with the lower dashed line using a constant Prandtl number of 1.0 and the upper dashed line using a table lookup of the Prandtl numbers predicted by CEA (Fig. 5). For the measured data, the oxidizer mass flow is calculated using the pressure difference across the injector assuming a discharge coefficient of 0.8. For the time-averaged regression rate data, the longitudinal average of the initial and final port cross-sectional area is used to normalize the mass flow calculation. For the instantaneous regression rate data, the cross-sectional area is calculated using the averaged regression rate from Table 3 integrated over time. The regression data from Table 2 is plotted as rectangular gray symbol, and the instantaneous midmotor regression data are plotted as open circles. Also plotted are test data for two motors that burn gaseous oxygen (GOX) and HTPB. These data are taken directly from Sutton and Biblarz ([3], pp. 591–592). The data are plotted here using English units so that the data from Sutton can be presented unaltered. Figure 23 shows that the regression rate model, especially when using the Prandtl number generated by CEA, shows remarkable agreement with the previously existing empirical data for the GOX/HTPB lab-scale motor and agrees well with the data obtained from the second N_2O/HTPB test firing.

VI. Conclusions

This paper develops a refined model for predicting hybrid motor fuel regression rates using an enthalpy-balance approach in which the ablation heat of the fuel grain is balanced by the convective heat transfer from the combustion flame zone to the fuel-grain surface. Currently, the rocket propulsion industry uses an empirical curve fit known as fit known as St. Robert's Law to predict the hybrid rocket fuel regression rates. This method requires multiple tests of a given fuel or grain configuration to determine the appropriate coefficients and these "after-the-fact" correlations do little to aid in the prediction of performance of new fuel formulations or grain designs. The

Table 3 Midmotor regression sensor data summary

Thermocouple pair	Δt, s	Absolute position in sensor array, cm	Δr from first TC in array, cm	Regression rate, cm/s
1,2	2.1667	0.000	0.2667	0.1260
2,3	2.8143	0.2667	0.3556	0.1264
1,3	4.0267	0.6223	0.6223	0.1275

Table 4 Parameters used for model calculations

Parameter	First test fire	Second test fire
Combustion port length, L	86.36 cm	86.36 cm
Combustion efficiency, η^*	95.0%	95.0%
Fuel density, ρ_{fuel}	866.0 kg/m^3	930.0 kg/m^3
Grain temperature, T_0	300.0 deg K	300.0 deg K
Heat of vaporization, h_v	1.8 MJ/Kg	1.8 MJ/Kg
Injector area, A_{ox}	0.35628 cm^2	0.35628 cm^2
Injector discharge coefficient, $C_{d_{\text{ox}}}$	0.27	0.8 with pipe losses
Initial port diameter	2.54 cm	5.08 cm
Nozzle throat area, A^*	5.067 cm^2	6.0 cm^2
Nozzle exit divergence angle	28.0 deg	28.0 deg
Nozzle expansion ratio	6.452	5.569
Oxidizer liquid density, ρ_{ox}	800.0 kg/m^3	800.0 kg/m^3

original enthalpy-balance regression model developed by Marxman has been modified to allow for nonunity Prandtl number. Because Prandtl number is a measure of the relative importance of skin friction and heat transfer within a viscous flow field, it has a significant effect on the resulting regression rates. When compared with experimental data, the regression model presented in this paper is shown to more accurately predict fuel regression rates for the 10.2 cm nitrous/HTPB motor and agrees well with previously generated data for GOX/HTPB motors. Given the regression rate prediction, the model also satisfactorily predicts the time varying chamber pressure, thrust, and specific impulse of the 10.2 cm motor. The authors feel that this model is an extension to industry standard practice for hybrid motor prediction and is a valuable tool to assist in calculating end-to-end motor performance. Clearly, the longitudinally averaged nature of the model is a limitation and extension to

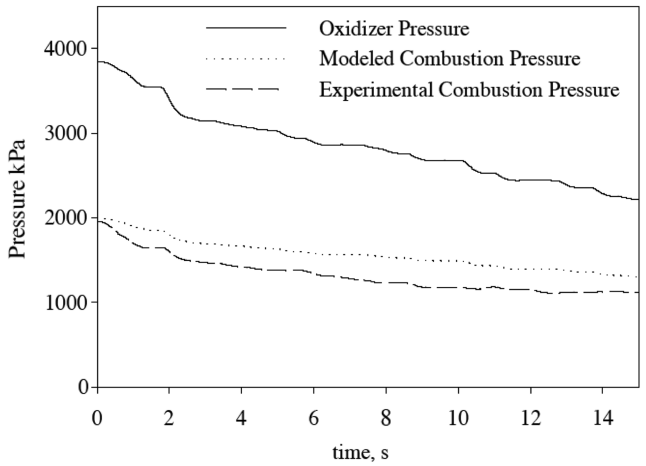

Fig. 18 Comparison of model predictions and measured value, combustion pressure, test 1.

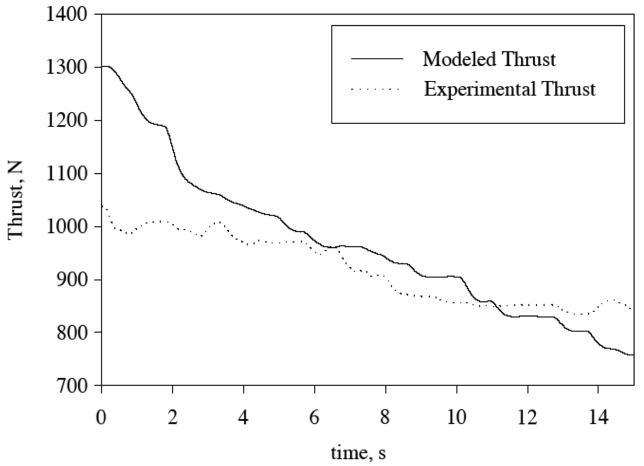

Fig. 20 Comparison of model predictions and measured value, thrust, test 1.

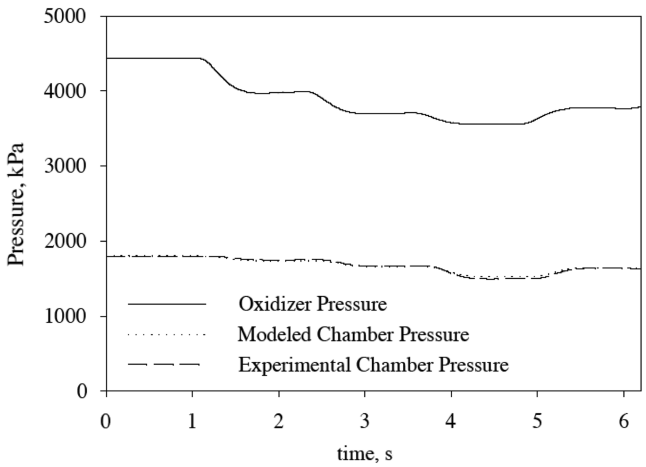

Fig. 19 Comparison of model predictions and measured value, combustion pressure, test 2.

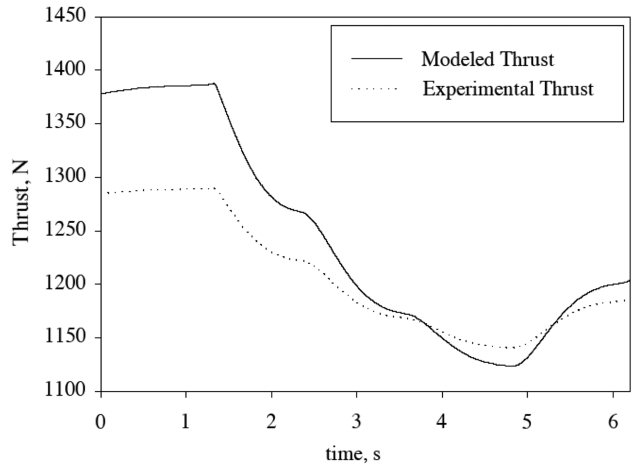

Fig. 21 Comparison of model predictions and measured value, thrust, test 2.

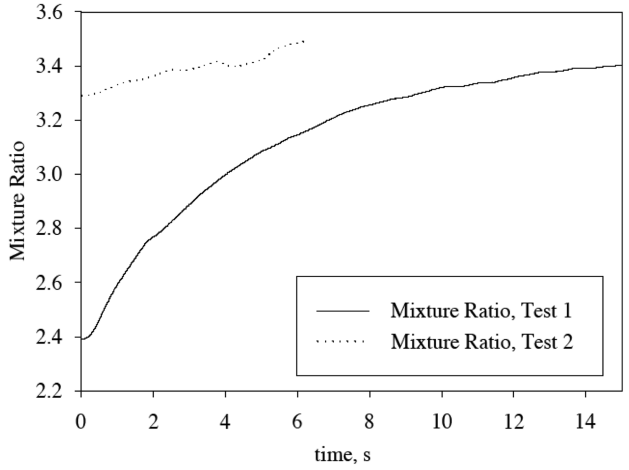

Fig. 22 Modeled burn mixture ratio from regression rate model, test 1 and test 2.

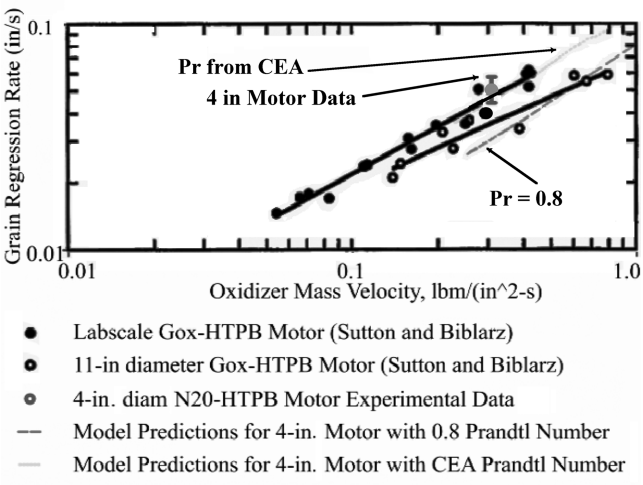

Fig. 23 Comparison of empirical and modeled HTPB fuel regression rates.

accommodate longitudinal variations in fuel regression rates is a logical next step for this modeling process.

References

[1] Chang, I., "Investigation of Space Launch Vehicle Catastrophic Failures," *Journal of Spacecraft and Rockets*, Vol. 33, No. 2, 1996, pp. 198–205. doi:10.2514/3.26741

[2] Anon., "Hazard Analysis of Commercial Space Transportation; Vol. 1: Operations, Vol. 2: Hazards, Vol. 3: Risk Analysis," U.S. Dept. of Transportation, PB93-199040, Accession No. 00620693, May 1988.

[3] Sutton, G. P., and Biblarz, O., *Rocket Propulsion Elements*, 7th ed., Wiley, New York, 2001, p. 10.

[4] Cheng, C. G., Farmer, R. C., Jones, H. S., and McFarlane, J. S., "Numerical Simulation of the Internal Ballistics of a Hybrid Rocket," AIAA Paper 94-0554, 1994.

[5] Chiaverini, M. J., Kuo, K. K., Peretz, A., and Harting, G., "Regression-Rate and Heat-Transfer Correlations for Hybrid Rocket Combustion," *Journal of Propulsion and Power*, Vol. 17, No. 1, Jan.–Feb. 2001, pp. 99–110.

[6] Strand, L. D., Ray, R. L., and Cohen, N. S., "Hybrid Rocket Combustion Study," AIAA Paper 93-2412, June 1993.

[7] Marxman, G., and Gilbert, M., *Turbulent Boundary Layer Combustion in the Hybrid Rocket*, Ninth Symposium on Combustion, Academic Press, New York, 1963, pp. 371–383.

[8] Marxman, G. A., Wooldridge, C. E., and Muzzy, R. J., "Fundamentals of Hybrid Boundary Layer Combustion," *Heterogeneous Combustion*, edited by H. G. Wolfdard, I. Glassman, and L. Green, Jr., Vol. 15, Progress in Astronautics and Aeronautics, Academic Press, New York, 1964, pp. 485–522.

[9] Easty, P., Altman, D., and McFarlane, J., "An Evaluation of Scaling Effects for Hybrid Rocket Motors," AIAA Paper 91-2517, June 1991.

[10] White, F. M., *Viscous Fluid Flow*, McGraw–Hill, New York, 1991, pp. 485–486.

[11] McCabe, W. L., Smith, J. C., and Harriot, P., *Unit Operations of Chemical Engineering*, 7th ed., McGraw–Hill, New York, 2004, pp 369–370.

[12] Crawford, M. E., and Kays, W. M., *Convective Heat and Mass Transfer*, McGraw–Hill, New York, 1993, p. 260.

[13] Lees, L., "Convective Heat Transfer with Mass Addition and Chemical Reactions," *Combustion and Propulsion*, 3rd AGARD Colloquium, Pergamon, New York, 1958, p. 451.

[14] White, F. M., *Viscous Fluid Flow*, 2nd ed., McGraw–Hill, New York, 1991, pp 550–552.

[15] Mottard, E. J., and Loposer, J. D., "Average Skin-Friction Drag Coefficients from Tank Tests of a Parabolic Body of Revolution," NACA RP-1161, 1957.

[16] Gordon, S., and McBride, B. J., "Computer Program for Calculation of Complex Chemical Equilibrium Compositions and Applications," NASA RP-1311, 1994.

[17] Zeleznik, F. J., and Gordon, S., "Calculation of Complex Chemical Equilibria," *Industrial & Engineering Chemistry*, Vol. 60, No. 6, 1968, pp. 27–57. doi:10.1021/ie50702a006

[18] Wingborg, N., "Increasing the Tensile Strength of HTPB with Different Isocyanates and Chain Extenders," *Polymer Testing*, Vol. 21, No. 3, 2002, pp. 283–287. doi:10.1016/S0142-9418(01)00083-6

[19] Marchese, A. J., "Work In Progress: This is Rocket Science: Development and Testing of a Hybrid Rocket Motor in a Rocket Propulsion Course," IEEE Paper 1-4244-0256, March–Oct. 2006, users.rowan.edu/~marchese/rockets05/hw6.doc [retrieved 14 June 2007].

[20] Ryan, P. W., "Polyurethane Based on Hydroxyl-Terminated Polybutadienes," *British Polymer Journal*, Vol. 3, No. 3, 1971, pp. 145–153. doi:10.1002/pi.4980030306

[21] Anon., PAPI 94 Technical Data Sheet, Dow Plastics Product Information, No. 109-00707-801XQRP, 2001.

[22] "NI Compact Fieldpoint," National Instruments, http://www.ni.com/compactfieldpoint/ [retrieved 18 June 2008].

[23] Beckwith, T. G., Marangoni, R. D., and Lienhard, V. J. H., *Mechanical Measurements*, 6th ed., Addison Wesley Longman, New York, 2006, pp. 43–73.

[24] Bendat, J. S., and Piersol, A. G., *Random Data: Analysis and Measurement Procedures*, Wiley-Interscience, New York, 1971, pp. 332–333.

T. Lin
Associate Editor